MATERIALS CHEMISTRY FRONTIERS

CHINESE CHEMICAL SOCIETY

ROYAL SOCIETY OF CHEMISTRY

RESEARCH ARTICLE

View Article Online
View Journal | View Issue

Cite this: *Mater. Chem. Front.*, 2021, **5**, 7276

Pyridyl-functionalized spiro[fluorene–xanthene] as a dopant-free hole-transport material for stable perovskite solar cells†

B. Yadagiri,‡[ab] Towhid H. Chowdhury,‡[c] Yulu He,[c] Ryuji Kaneko,[c] Ashraful Islam *[c] and Surya Prakash Singh *[ab]

Received 19th March 2021,
Accepted 21st July 2021

DOI: 10.1039/d1qm00435b

rsc.li/frontiers-materials

Hole-transport materials (HTMs) play a critical role in perovskite solar cells (PSCs) for achieving high efficiency and stability. Herein, we have designed and synthesized an HTM named SPS-SPX-2TPA and studied its photovoltaic performance for PSC applications. The molecule SPS-SPX-2TPA consists of pyridyl substitution at *para*-position attached with a spiro[fluorene-9,9′-xanthene] (SFX) moiety as a central core unit and finally end capped with an *N*,*N*-dimethoxytriphenylamine (TPA) moiety. The synthesized SPS-SPX-2TPA HTM is three times cheaper than the most commonly used Spiro-OMeTAD HTM. Mesoporous PSCs fabricated using SPS-SPX-2TPA as the HTM showed the best power conversion efficiency (PCE) of 17.39% and 16.22% (device area 0.10 cm^2) in forward and reverse bias, respectively. Moreover, the SPS-SPX-2TPA-based PSCs showed a stable photovoltaic performance of up to 270 h when measured under light soaking and maintained 95% of their initial PCE even after 600 h when measured under maximum power point tracking conditions with high reproducibility.

Introduction

Among the third generation solar cell technologies perovskite solar cells (PSCs) have shown a rapid rise in power conversion efficiency (PCE) over the past decade.[1,2] PSCs have diverse advantages over generic solar cells such as solution processability, efficient ambipolar charge diffusion, a long charge-carrier diffusion length, and strong panchromatic absorption properties.[3,4] Aside from the perovskite as the main light-absorber layer, state-of-the-art PSC devices consist of different charge-carrier layers such as hole-transporting materials (HTMs), electron-transporting layers (ETLs) and counter electrode layers (cathode and anode). PSCs devices with a typical mesoporous structure, the perovskite active layer is sandwiched between the mesoporous TiO_2 layer and HTM.[5] Since the inception of PSCs, remarkable development from 3.8% PCE to the state-of-the-art 25.6% PCE has been achieved *via* device engineering,[6] perovskite configuration tuning,[7] and structural modification of the charge-carrier layers (the HTM and the ETL).[8] Among many other crucial factors, HTMs play an important role to extract holes effectively from the photo-induced perovskite absorber as well as transporting holes to the adjacent counter electrode.[5] Furthermore, the HTM layer should be stable against ambient moisture to protect the perovskite layer. Numerous scientific approaches have focused on developing HTMs that have suitable optical, electrochemical and photo-physical properties such as absorption, matched energy levels with the respective perovskite absorbers, high charge mobility, and high conductivity.[9–13]

The well-known and most efficient small molecular HTM in PSCs is 2,2′,7,7′-tetrakis-(*N*,*N*-di-*p*-methoxyphenylamino)-9,9′-spiro-bifluorene (Spiro-OMeTAD) because of its amorphous character, solubility in common organic solvents and excellent photovoltaic performance. Although Spiro-OMeTAD-based PSCs show a high photovoltaic response,[14] they suffer from several drawbacks, such as less hole conductivity, and tedious synthesis and purification procedures, which make them very expensive.[15] Additionally, to increase the conductivity, steady-state performance[16] and stability, Spiro-OMeTAD-based HTMs are often doped with various hygroscopic materials, namely-bis(trifluoromethane)sulfonimide lithium salt (LiTFSI) and 4-*tert*-butylpyridine (*t*BP). Both LiTFSI and *t*BP act as a p-type dopant and a recombination-blocking agent, respectively.[17] The effect of LiTFSI and *t*BP dopants in PSCs has been well explained by Snaith *et al.* in 2017.[18] Their study revealed that

[a] *Polymers and Functional Materials Division, CSIR-Indian Institute of Chemical Technology (IICT), Uppal road, Tarnaka, Hyderabad, 500007, India. E-mail: spsingh@iict.res.in*
[b] *Academy of Scientific and Innovative Research (AcSIR), Ghaziabad, Uttar Pradesh, India*
[c] *Photovoltaic Materials Group, Center for Green Research on Energy and Environmental Materials, National Institute for Materials Science (NIMS), 1-2-1 Sengen, Tsukuba, 305-0047, Ibaraki, Japan. E-mail: ISLAM.Asharful@nims.go.jp*

† Electronic supplementary information (ESI) available. See DOI: 10.1039/d1qm00435b

‡ These authors contributed equally.

the outstanding improved performance of PSCs was due to the direct contact between the *t*BP and the perovskite, which influences the HTM/perovskite interface to promote enhanced hole collection. Furthermore, existence of *t*BP seems to have cause p-doping on the surface of the perovskite film, facilitating more superior diode refinement.[18] Meng *et al.* revealed that *t*BP acts as a morphology regulator for HTMs to outstandingly increase the homogeneity and control the aggregation of LiTFSI.[19] However, the low boiling point (196 °C) of *t*BP facilitates quick evaporation during fabrication of the PSCs. This can hugely impact the long-term stability and reproducibility. Furthermore, *t*BP has a tendency to decompose the perovskite active layer to form a PbI_2 complex that hinders the charge transport between the HTM and the adjacent perovskite.[20]

Due to the issues arising from the dopants in the HTMs, numerous studies on the development of novel low-cost small molecular HTMs using different types of central core moieties, such as carbazole,[21] pyrene,[22] triphenylamine,[23] triazatruxene,[24,25] phenothiazine,[26] benzothiadiazole,[27] dithienosilole,[28] dithienogermole[10] and spiro-fluorene-9-9′-xanthene (SFX),[19,29,30] have been systematically carried out using molecular engineering approaches. Licheng Sun *et al.* reported SFX-based HTMs (see Fig. 1(I and II)) for planar PSCs with PCE of over 20%.[29] Alex K.-Y. Jen *et al.* reported SFX-based dopant-free HTMs (see Fig. 1(III and IV)) for planar PSCs with a PCE of ~21%.[19] The structure of the SFX moiety is similar to that of the spiro-fluorene (existing in Spiro-OMeTAD) moiety and it is differentiated by one oxygen atom. Due to the perpendicular structure of SFX-based materials, they can efficiently prevent intermolecular π–π interactions with more solubility in common organic solvents and form a good amorphous homogeneous layer to efficiently extract holes from the adjacent perovskite layer. Additionally, HTMs consisting of a pyridine unit can deliver the long-term stability of PSCs compared with doped Spiro-OMeTAD.[31,32] Incorporation of the pyridine unit in HTMs can increase the binding capacity and improve the interfacial connection between the HTM and the perovskite, passivate the surface traps over pyridine substitution and decrease the charge recombination of the active layer.

In this study, we report on the design and synthesis of pyridine-functionalized SFX moieties as dopant-free HTMs for PSCs. The chemical structure of the synthesized SPS-SPX-2TPA is shown in Fig. 1. The symmetric SPS-SPX-2TPA consists of *para*-position-substituted pyridines attached to the SFX moiety as a central building block and both sides end capped with the TPA moiety. This molecule shows suitable optical and electrochemical properties, such as strong and broad absorption in the visible region, highest occupied molecular orbital (HOMO)

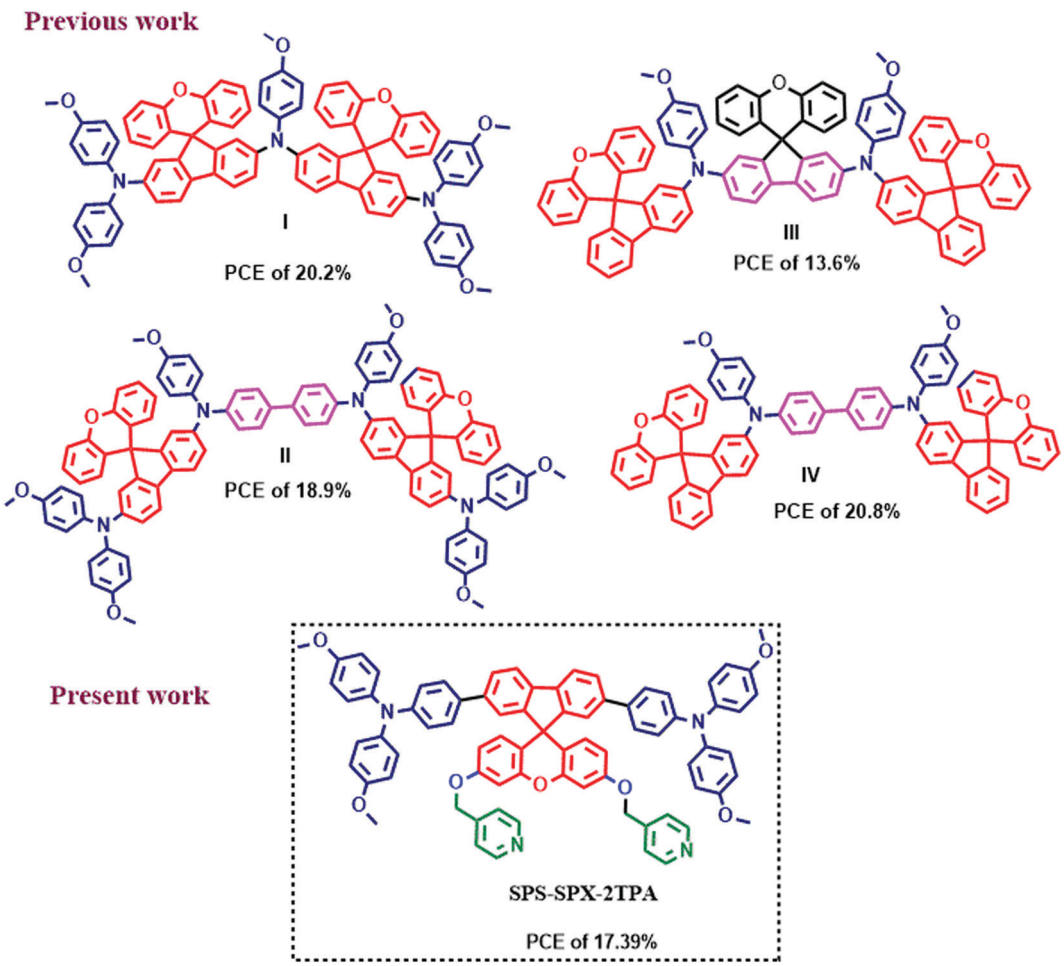

Fig. 1 Present and previous work on SFX-based HTMs in PSCs.

and the lowest unoccupied molecular orbital (LUMO) energies of −5.08 eV and −2.19 eV, respectively, and a high conductivity of 3.49×10^{-5} S cm^{-1}. PSCs were fabricated using SPS-SPX-2TPA as the HTM, which exhibited a PCE of 17.39% under reverse bias conditions for mesoporous $CH_3NH_3PbI_3$-based PSCs measured under 100 mW cm^{-2} (AM 1.5G sun illumination). Additionally, the PSCs showed high reproducibility and did not lose any photovoltaic performance when measured under continuous light soaking for up to 270 h, maintaining 95% of its initial PCE even after 600 h when measured under maximum power point tracking conditions at room temperature. Some of the previous works of SFX-based HTMs for perovskite solar cells are shown in Fig. 1.

Results and discussion

Synthesis and characterization

The molecular arrangement and synthetic route for SPS-SPX-2TPA are shown in Scheme 1, and complete experimental details and characterization are shown in the ESI.† The intermediate **III** was synthesized according to a previous literature report.[33] Intermediate **1** was prepred from 2,7-dibromofluorenone and resorcinol in the presence of *p*-toluenesulfonic acid (PTSA) as a catalyst in toluene, which resulted in a 75% product yield. The intermediate **2** was prepared *via* a nucleophilic substitution reaction between 4-(chloromethyl)pyridine and intermediate **1** in the presence of cesium carbonate (Cs_2CO_3) as a base, in acetonitrile solvent in 75% yield. Finally, SPS-SPX-2TPA was prepared from intermediate **2** and intermediate **III** *via* a Stille-coupling reaction using $Pd(dba)_3$ as the catalyst and $P(o\text{-toly})_3$ as the ligand in dry toluene for 48 h, in 61% yield. Due to the presence of the methoxy groups in the SPS-SPX-2TPA molecules, excellent solubility in common organic solvents such as chlorobenzene (CB), chloroform ($CHCl_3$), dichloromethane (DCM) and *o*-dichlorobenzene (*o*-DCB) was observed. For purification of all the intermediates and the final compound, we used silica gel of different mesh sizes (60–120, 100–200 and 230–400) and column chromatography, and the chemical structures were fully characterized by the ^1H, ^{13}C NMR and mass spectra, and the complete details of these spectra are shown in the ESI.†

UV-visible absorption spectra

To understand the absorption behaviour of the SPS-SPX-2TPA molecule in both the solution and solid state we studied the UV-visible absorption spectra in both $CHCl_3$ solution

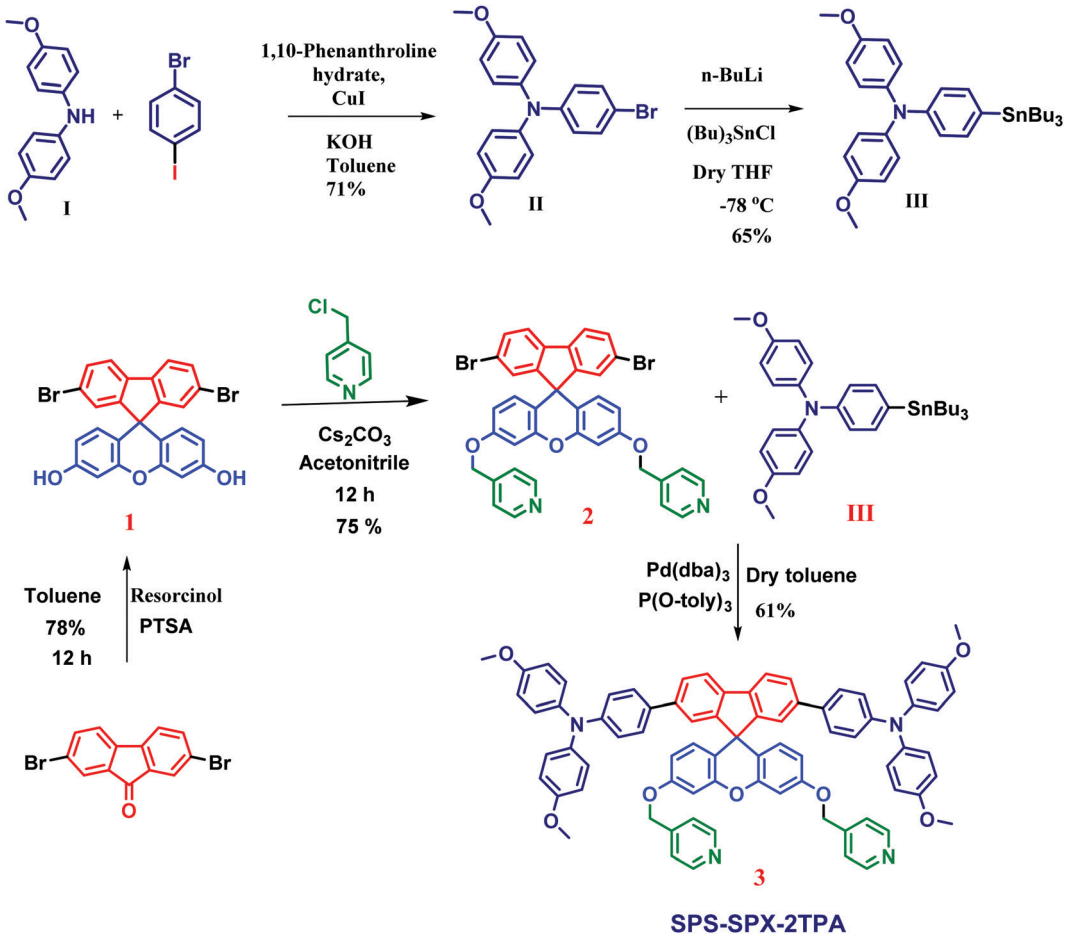

Scheme 1 Synthesis route for the SPS-SPX-2TPA hole-transporting material.

(1×10^{-5} M concentration) and as thin films, as shown in Fig. 2, and the corresponding results are shown in Table 1. In the solution state (Fig. 2a), both SPS-SPX-2TPA and Spiro-OMeTAD show strong and broad absoption from the UV to the visible region covering 300–450 nm. The strong absorption peaks at 370 nm (ε = 94 327 M^{-1} cm^{-1}) and 386 nm (ε = 100 837 M^{-1} cm^{-1}) are due to intramolecular charge transfer (ICT) transitions among the donors and acceptors present in the molecules. Fig. 2b represents the molar extinction coefficient (ε) spectra of both molecules. As per Fig. S1 (ESI†), the thin-film absoption spectrum of the SPS-SPX-2TPA molecule showed a strong and broad absorption at 400 nm (ε = 53 480 M^{-1} cm^{-1}) and an absorption onset up to 600 nm (NIR region). Compared with the solution state, the thin-film absorption was redshifted by up to 30 nm because of the strong π–π intermolecular stacking in the solid state. The optical band gap of the SPS-SPX-2TPA molecule was observed at 2.74 eV, which is calculated from the onset absorption (λ_{onset} = 452 nm) from the thin-film absorption spectrum. As per the above results, we found that both the wavelength maximum and the band gaps of the SPS-SPX-2TPA molecule were similar to those of Spiro-OMeTAD.

Cyclic voltammetry

To examine the redox properties such as the HOMO and LUMO of the SPS-SPX-2TPA molecule, we conducted cyclic voltammetry (CV) and differential pulse voltammetry (DPV) at room temperature under inert nitrogen conditions using dry dichloromethane (DCM) solution with a suitable supporting electrolyte (0.1 M of tetrabutylammonium perchlorate (TBAF)). The CV study results using a ferrocene/ferrocenium (Fc/Fc^+) redox couple as standard and results are tabulated in Table 1. In Fig. 3a, SPS-SPX-2TPA shows one oxidation and one reduction potential peak. The HOMO energy level of SPS-SPX-2TPA was determined to be −5.08 eV, which is calculated from the $E_{HOMO} = -e[E_{ox} + 4.80 - E(Fc/Fc^+)]$ equation. The LUMO energy level of SPS-SPX-2TPA was determined to be −2.19 eV, calculated from the $E_{LUMO} = -e[E_{red} + 4.80 - E(Fc/Fc^+)]$ equation. The reason for the lower HOMO and LUMO energy levels for SPS-SPX-2TPA is due to the high electron-donating character of the SFX unit. The HOMO and LUMO levels of the SPS-SPX-2TPA molecule were on a par with those of the Spiro-OMeTAD molecule. The energy level diagram of a PSC with SPS-SPX-2TPA as HTM is shown in Fig. 3b.

To obtain a high photovoltaic response, the suitable HTM should have a high conductivity and a high hole mobility, which are useful for decreasing the losses during hole transport to the corresponding electrode. The conductivity (σ) of SPS-SPX-2TPA was calculated using eqn (1)–(3).[9]

$$R = V/J \quad (1)$$

$$\rho = RXA/L \quad (2)$$

$$\sigma = 1/\rho \quad (3)$$

In the above equations, voltage (V) and current (J) are calculated from the J–V spectra of the hole-only devices. The resistance (R), conductor surface area (A), electrical resistivity (ρ), and pathlength (L) of the conductor were calculated using the ellipsometry optical technique. To scrutinize the vertical conductivity

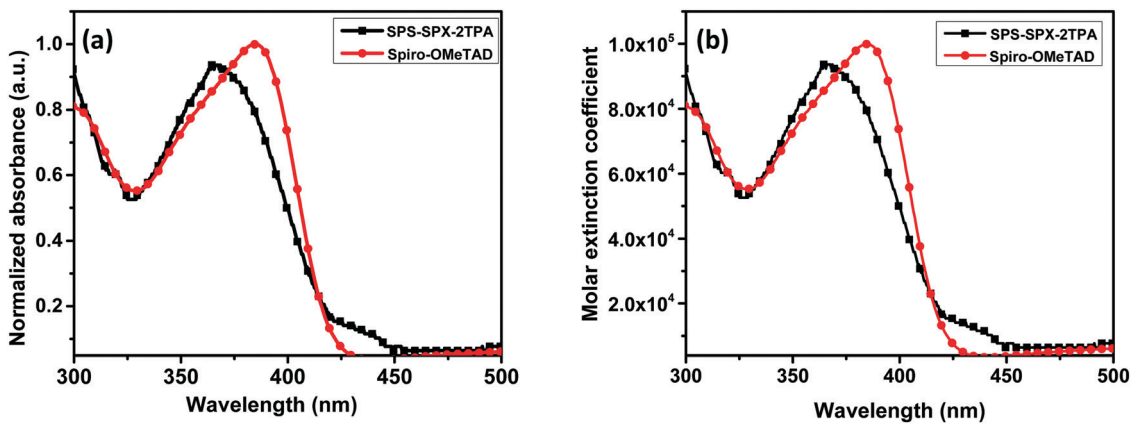

Fig. 2 (a) UV-visible absorption spectra in solution and (b) molar extinction coefficient spectra of both SPS-SPX-2TPA and Spiro-OMeTAD molecules.

Table 1 Optoelectronic properties of SPS-SPX-2TPA and Spiro-OMeTAD

HTM	$\lambda_{max}(nm)_{sol}$[a] (ε M^{-1} cm^{-1})	λ_{max}[b] $(nm)_{film}$	$\lambda_{onset\ (film)}$	E_g^{opt} (eV)[c]	HOMO[d] (eV)	LUMO[d] (eV)
SPS-SPX-2TPA	370 (94 327)	400	452	2.71	−5.08	−2.19
Spiro-OMeTAD	386 (100 837)	406	419	3.05	−5.13	−2.08

[a] Calculated in $CHCl_3$ solution state. [b] Film fabricated from $CHCl_3$ solution. [c] Optical bandgap measured from the wavelength (λ_{onset}) of the solid-state absorption. [d] HOMO = $-(4.80 - E_{1/2},Fc/Fc^+ + E_{ox})$ (eV); LUMO = $-(4.80 - E_{1/2},Fc/Fc^+ + E_{red})$ (eV) *via* Ag/AgCl as the reference electrode.

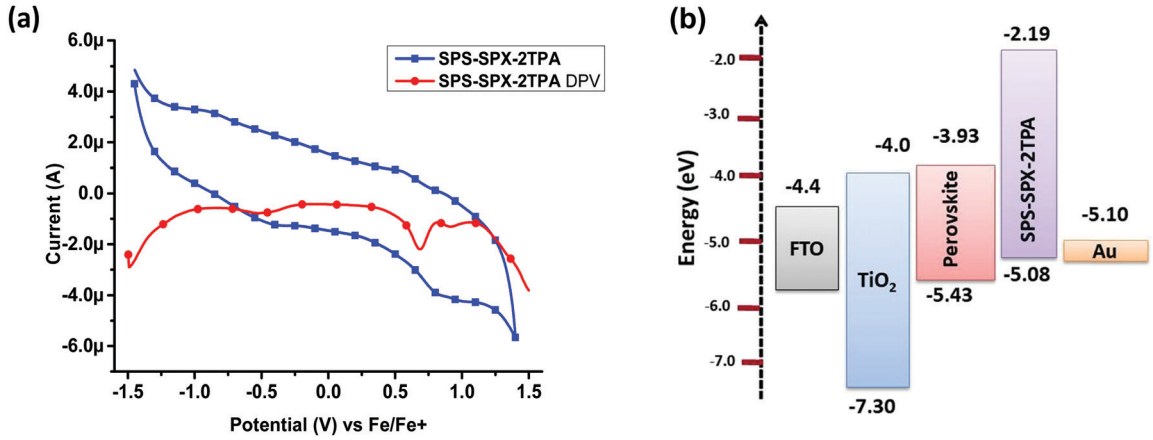

Fig. 3 (a) CV and DPV spectra of SPS-SPX-2TPA. (b) Energy level diagram of a PSC with SPS-SPX-2TPA as the HTM.

of the SPS-SPX-2TPA HTM, hole-only devices were fabricated by using the ITO/PEDOT:PSS/HTM/Au device architecture (see Fig. S2a, ESI†), resulting in a conductivity of 3.49×10^{-5} S cm^{-1}, which was higher than the conductivity of Spiro-OMeTAD doped with *t*BP and LiTFSI (8.37×10^{-6} S cm^{-1}). The conductivity result of SPS-SPX-2TPA is attributed to the highly conjugated unit in the material and to enhanced π–π stacking in the solid state. To further understand the electronic properties of SPS-SPX-2TPA, we measured the hole mobility based on space charge limited current (SCLC) measurements using the hole-only devices (see Fig. S2a, ESI†), which was calculated using the Mott–Gurney law.[35] The *J*–*V* curves of the respective hole-only devices are shown in Fig. S2b (ESI†). The hole mobility of SPS-SPX-2TPA without any dopants was calculated to be 8.28×10^{-4} cm^2 V^{-1} s^{-1}, whereas the hole mobility of Spiro-OMeTAD with dopants (*t*BP and LiTFSI) was calculated to be 1.90×10^{-4} cm^2 V^{-1} s^{-1}. With the aid of the higher conductivity and hole mobility in dopant-free SPS-SPX-2TPA compared with doped Spiro-OMeTAD it is expected that SPS-SPX-2TPA can perform as a dopant-free HTM for PSCs.

Theoretical study

We computed density functional theory (DFT) calculations for further understanding the structural, electronic, and charge-transporting properties of the SPS-SPX-2TPA HTM. The top and side views of SPS-SPX-2TPA and Spiro-OMeTAD are shown in Fig. 4a and b. The optimized geometry of SPS-SPX-2TPA exhibited a highly twisted non-planar molecular structure in which the pyridine-substituted xanthene core in a single plane, enabling the molecules to be tightly packed. The methoxy-substituted phenyl rings of the triphenylamines are twisted out of the plane, promoting the solubility of the SPS-SPX-2TPA molecule in traditional organic solvents, thereby making a very smooth thin film. Furthermore, the HOMOs of SPS-SPX-2TPA is delocalized throughout the central fluorene core but with the majority on the terminal TPA units, while the LUMOs are placed on the pyridine-substituted xanthene core. Therefore, ample orbital overlap between the HOMOs and LUMOs indicates that there may be the rapid creation of neutral excitons and the transition of hole transfer. The HOMO energy levels of SPS-SPX-2TPA and Spiro-OMeTAD also suggest that SPS-SPX-2TPA has a deeper HOMO level than that of Spiro-OMeTAD (see Fig. 5a), demonstrating its suitability with the HOMO level of the perovskite (−5.43 eV).

It has been suggested that the HTM plays a key role in controlling the stability of PSCs. To assess the stability of SPS-SPX-2TPA, the absolute hardness (η) and the electrostatic surface potential (ESP) were considered, and the results are presented in Table 3 and depicted in Fig. 5b. The absolute hardness is estimated by $n = (IP_a - EA_a)/2$ where, IP_a and EA_a

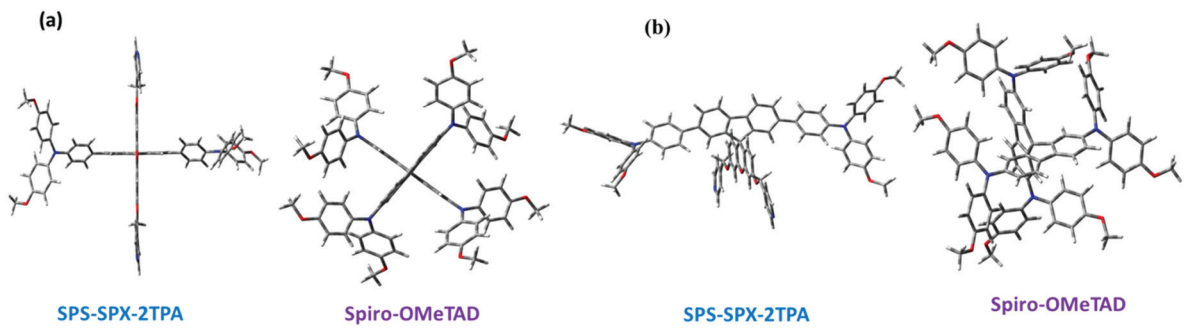

Fig. 4 Top and side views of SPS-SPX-2TPA and Spiro-OMeTAD.

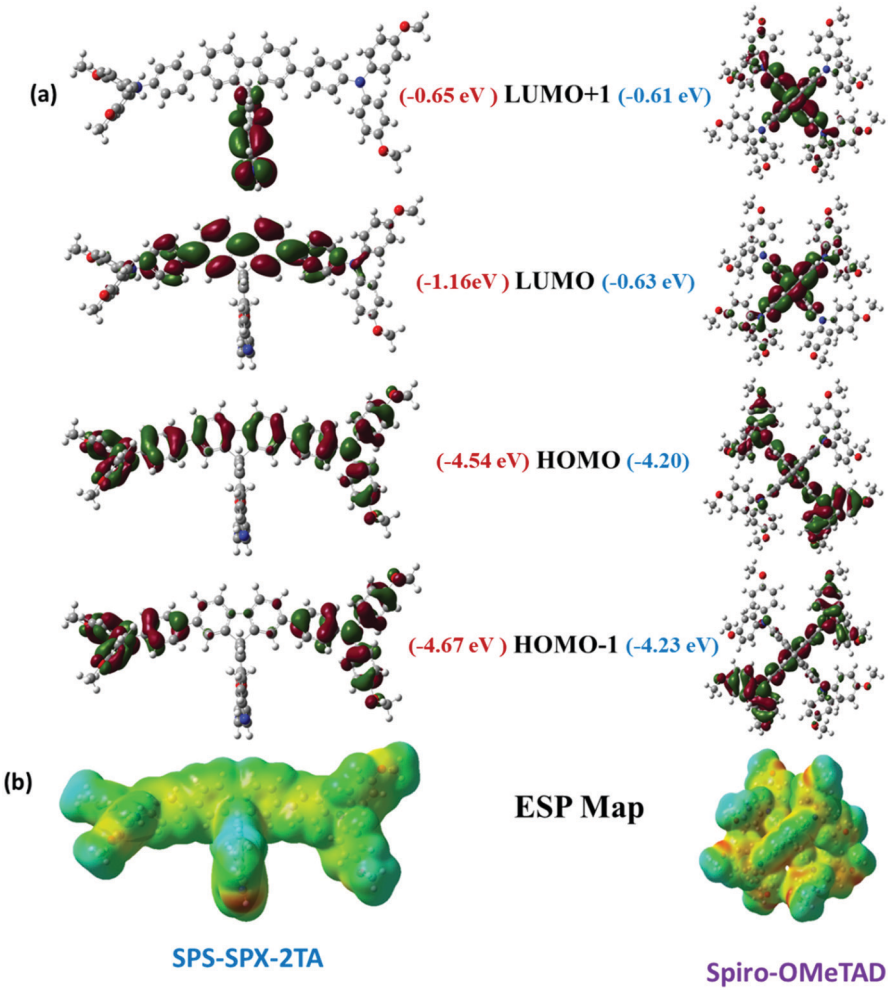

Fig. 5 The schematic representation of energy levels (a) and electrostatic surface potential (b) of both SPS-SPX-2TPA and Spiro-OMeTAD HTMs.

are the adiabatic ionization potential and the electron affinity, respectively. The calculated n values for SPS-SPX-2TPA and Spiro-OMeTAD are 2.24 and 2.40 eV, respectively, indicating that the planarity of the core structure can effectively enhance the stability of the HTMs. The electrostatic surface potential (ESP) (Fig. 5b) reveals the electronegative character of the nitrogen in both the pyridine units present on the xanthene core, while the most electropositive portion is much more spread out over the molecule. We observed a clear directional dipole in SPS-SPX-2TPA ($\mu_g \approx 4.44$ Debye) and Spiro-OMeTAD ($\mu_g \approx 2.91$ Debye). This strong dipole in the unit could assist molecular packing in the film, which is expected to augment the intermolecular charge transport. In general, the more negative charges on the molecule promote the ease of oxidation, thereby decreasing the molecular stability. Thus, SPS-SPX-2TPA is more stable than Spiro-OMeTAD. These findings are in good accord with the absolute hardness values. Additionally, we estimated the charge-transport phenomena, *i.e.*, the hole and electron reorganization energies, presented in Table 2 (see in Table S1 in ESI†). According to Marcus theory, the reorganization energy (λ) is one of the significant parameters for estimating the hole-transport phenomena in HTMs, and a lower λ_{hole} value is helpful in facilitating the hole transport. The reorganization energies of SPS-SPX-2TPA and Spiro-OMeTAD are 0.132 eV and 0.149 eV, respectively. The decreased λ values, which display an adverse influence on the hole-hopping rate in comparison with that of the transfer integrals, will be favourable for promoting hole transport to

Table 2 Theoretical energy levels and charge-transport parameters

HTM	HOMO	LUMO	E_g	μ_{dipol}	IP_a	EA_a	η	λ_+	λ_-	Transporter
SPS-SPX-2TPA	−4.54	−1.16	3.38	4.44	5.21	0.73	2.24	0.132	0.519	Hole ($\lambda_+ < \lambda_-$)
Spiro-OMeTAD	−4.20	−0.63	3.57	2.91	4.85	0.05	2.40	0.149	0.329	Hole ($\lambda_+ < \lambda_-$)

(Here, μ_{dipol} is given in Debye and other parameters are in eV).

the adjacent perovskite layer. Time-dependent density functional theory (TDDFT) studies for both SPS-SPX-2TPA and Spiro-OMeTAD hole-transporting materials are discussed in the ESI† (see Fig. S3).

Photovoltaic performance

With these favorable optoelectronic properties of the SPS-SPX-2TPA molecule, we fabricated PSCs using SPS-SPX-2TPA as a dopant-free HTM. The PSCs were fabricated with the device structure of FTO/comp-TiO_2/mp-TiO_2/$CH_3NH_3PbI_3$/(SPS-SPX-2TPA/Spiro-OMeTAD)/Au. The surface morphology of the $CH_3NH_3PbI_3$ obtained by scanning electron microscopy (SEM) is shown in Fig. S4a (ESI†). The perovskite layer showed a smooth surface with large grains. The spin-coated film of SPS-SPX-2TPA on top of the $CH_3NH_3PbI_3$ is shown in Fig. S4b (ESI†), and shows full coverage over the perovskite film. Fig. 6a shows the current density–voltage (J–V) curves of the PSCs fabricated using SPS-SPX-2TPA and Spiro-OMeTAD as the HTM, measured at forward and reverse bias under AM 1.5G conditions, and the respective photovoltaic parameters are summarized in Table 3. The best PSCs fabricated using dopant-free SPS-SPX-2TPA showed a PCE of 17.39%, with an open-circuit voltage (V_{OC}) of 1.15 V, a short-circuit current density (J_{SC}) of 20.72 mA cm^{-2}, and a fill factor (FF) of 73% under the reverse bias condition. A PCE of 16.22%, with a V_{OC} of 1.13 V, a J_{SC} of 20.81 mA cm^{-2} and an FF value of 69%, was achieved under the forward bias condition. Under the same scanning conditions, the Spiro-OMeTAD-based PSC showed a PCE of 18.29%, with a V_{OC} of 1.07 V, a J_{SC} of 22.21 mA cm^{-2} and an FF of 77% under the reverse bias condition; the forward bias condition gave a PCE of 17.52% with a V_{OC} of 1.09 V, a J_{SC} of 21.73 mA cm^{-2} and an FF of 74%. The hysteresis index (HI) [HI = ($PCE_{Reverse}$ − $PCE_{Forward}$)/$PCE_{Reverse}$] values for both the PSCs fabricated using SPS-SPX-2TPA and Spiro-OMeTAD were measured. The SPS-SPX-2TPA-based PSC showed an HI of 0.06, which was a little higher than that of the Spiro-OMeTAD-based PSC (HI = 0.04). Fig. 6b represents the incident photon-to-electron conversion efficiency (IPCE) spectra of both SPS-SPX-2TPA and Spiro-OMeTAD HTMs. Both materials showed similar IPCE spectra and achieved an IPCE value of up to 80%.

Table 3 Photovoltaic parameters of the PSCs fabricated using SPS-SPX-2TPA and Spiro-OMeTAD HTMs

HTM	Scan direction	J_{sc} (mA cm^{-2})	V_{OC} (V)	FF (%)	PCE (%)	HI
SPS-SPX-2TPA	Forward bias	20.81	1.13	69	16.22	0.06
	Reverse bias	20.72	1.15	73	17.39	
Spiro-OMeTAD	Forward bias	21.73	1.09	74	17.52	0.04
	Reverse bias	22.21	1.07	77	18.29	

To understand the influence of the SPS-SPX-2TPA-based HTM on the performance of the fabricated PSCs, steady-state photoluminescence (PL) (Fig. S5a, ESI†) and time-resolved photoluminescence (TRPL) (Fig. S5b, ESI†) measurements were obtained and are shown in the ESI.† To avoid the quenching contribution from TiO_2 and mesoporous TiO_2 layers, all the respective PL and TRPL measurements were carried out on bare glass substrates. The glass/perovskite film showed high photoluminescence, which confirms the superior quality of the fabricated $CH_3NH_3PbI_3$ film. For the $CH_3NH_3PbI_3$/Spiro-OMeTAD and $CH_3NH_3PbI_3$/SPS-SPX-2TPA films, stronger quenching was observed compared with that of using only SPS-SPX-2TPA. The higher steady-state PL quenching with SPS-SPX-2TPA clearly indicates more efficient charge transfer from the $CH_3NH_3PbI_3$ layer, which is on a par with the hole-mobility measurements. To further evaluate the mechanism behind the charge-transfer process, we have evaluated the TRPL performance of the respective films. The $CH_3NH_3PbI_3$-based films showed an average lifetime of 379.36 ns. The average lifetime of the $CH_3NH_3PbI_3$/Spiro-OMeTAD films was reduced to 268.62 nS and the average lifetime of the $CH_3NH_3PbI_3$/SPS-SPX-2TPA-based films was reduced to 256.8 nS.

Durability and reproducibility of the PSCs

The long-term stability (durability) of PSC devices, a key parameter for PSCs, was measured. We conducted stability testing of un-encapsulated PSCs using SPS-SPX-2TPA and

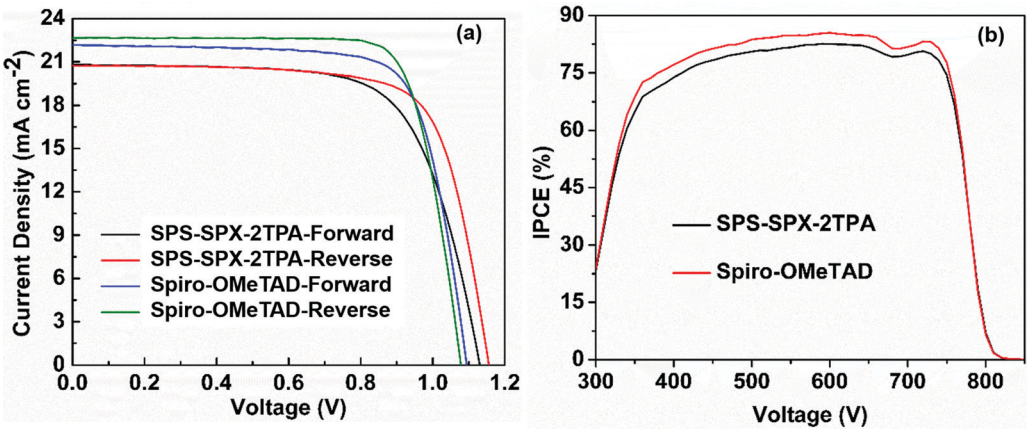

Fig. 6 (a) J–V and (b) IPCE spectra under light illumination of the PSCs fabricated using SPS-SPX-2TPA and Spiro-OMeTAD.

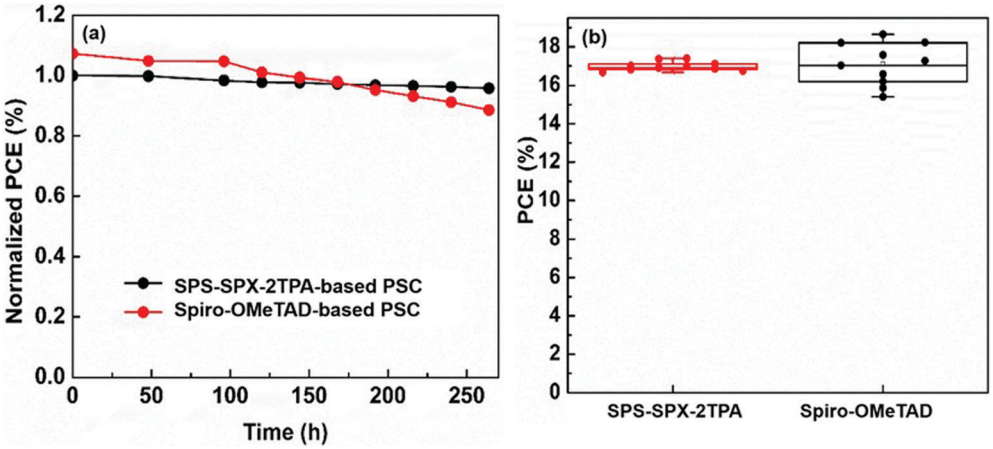

Fig. 7 (a) Light-soaking stability under light illumination and (b) reproducibility of the PSCs fabricated using SPS-SPX-2TPA and Spiro-OMeTAD.

Spiro-OMeTAD as the HTM under 50% humidity conditions. The photovoltaic perfomance of the PSC devices was measured over a period of 270 h to observe their performance over the long term, as shown in Fig. 7a. During the 200th hour, the Spiro-OMeTAD HTM-based PSC showed a notable decline from its initial efficiency. Intersitingly, the SPS-SPX-2TPA HTM-based PSC device did not degrade at all and showed stable photovoltaic behavior, maintaining its initial PCE. From this observation, it was clear that our devoloped SPS-SPX-2TPA HTM is a great candidate for highly stable PSCs. As per the reported literature,[34] usually, PCE hysteresis in PSCs can occur due to the localization of positively charged ions at the interface among the perovskite active layer and electron-transport layer (ETL). This can be credited to the acceleration of non-radiative recombination, and resuts in degradation of the PSCs because of the effects of localized possitive ions. To further understand the stability behaviour of our HTM for PSCs, we carried out stabilized measurements. The stabilized J_{SC} was observed to be 19.85 mA cm^{-2} for the SPS-SPX-2TPA-based PSCs, whereas a stabilized J_{SC} was observed at 19.67 mA cm^{-2} for the Spiro-OMeTAD-based PSC (please see Fig. S6, ESI†). It is noticable that at the initial stage the J_{sc} of the Spiro-OMeTAD-based PSC was higher, but the stabilized J_{SC} was higher for the SPS-SPX-2TPA-based PSC. We also measured the steady-state PCE of the PSCs fabricated using SPS-SPX-2TPA and Spiro-OMeTAD at maximum a power point of 0.860 V. For the SPS-SPX-2TPA-based PSC, a steady-state PCE of 12.08% was observed, and the Spiro-OMeTAD-based PSC showed a PCE of 12.03% (please see Fig. S7, ESI†). Note that the stabilized PCE of the SPS-SPX-2TPA-based PSC was a little higher. Motivated by these results we studied the stability at the maximum power point tracking (MPPT) of the respective PSCs under 1 Sun and at room temperature for a period of 600 h (Fig. S8, ESI†). Under MPPT conditions, after 100 h the Spiro-OMeTAD-based PSC started to degrade and loses up to 60% of its initial performance within the measured 600 h. However, the SPS-SPX-2TPA-based PSC maintained 95% of its initial PCE even after 600 h. We also conducted a reproducibility study of the PSCs fabricated using both SPS-SPX-2TPA and Spiro-OMeTAD HTMs in order to understand the commercialization aspects of these PSCs. As shown in Fig. 7b, the SPS-SPX-2TPA-based PSC showed high reproducibility with minimum variation of the PCE compared with that of the Spiro-OMeTAD-based PSC.

Conclusion

In conclusion, we have synthesised a new pyridyl-functionalized spiro[fluorene–xanthene]-based hole-transporting material (SPS-SPX-2TPA), considering the cost of well-known Spiro-OMeTAD for dopant-free perovskite solar cells. The synthesized SPS-SPX-2TPA is three times cheaper than Spiro-OMeTAD. This molecule shows suitable optical and electrochemical properties, such as broad absorption in the UV and visible regions, suitable HOMO and LUMO energies (−5.08 eV and −2.19 eV, respectively), a high conductivity of 3.49×10^{-5} S cm^{-1} and a hole mobility of 8.28×10^{-4} cm^2 V^{-1} s^{-1}. Under dopant-free conditions, a PCE of 17.39% and 16.22% was achieved in both reverse and forward bias, respectively (device area 0.10 cm^2). Moreover, SPS-SPX-2TPA-based PSCs show stable thermal photovoltaic behaviour when measured under MPPT conditions. The current study proposes that the design and synthesis of novel pyridine-functionalized SFX-based hole-transporting materials certainly might be a solution to achieve highly stable and efficient perovskite solar cells.

Conflicts of interest

There are no conflicts to declare.

Acknowledgements

B. Y. thanks UGC for providing a senior research fellowship. S. P. S. acknowledges financial support from DST-SERB (EMR/2017/001506). CSIR-IICT Communication No.: IICT/Pubs./2020/372. A. I. acknowledges the support from JSPS KAKENHI Grant No. 18H02079.

References

1 J. Y. Shao, N. Yang, W. Guo, B. Bin Cui, Q. Chen and Y. W. Zhong, Introducing fluorene into organic hole transport materials to improve mobility and photovoltage for perovskite solar cells, *Chem. Commun.*, 2019, **55**, 13406–13409.

2 S. Maddala, C. L. Chung, S. Y. Wang, K. Kollimalayan, H. L. Hsu, P. Venkatakrishnan, C. P. Chen and Y. J. Chang, Forming a metal-free oxidatively coupled agent, bicarbazole, as a defect passivation for htm and an interfacial layer in a p–i–n perovskite solar cell exhibits nearly 20% efficiency, *Chem. Mater.*, 2020, **32**, 127–138.

3 S. D. Stranks, G. E. Eperon, G. Grancini, C. Menelaou, M. J. P. Alcocer, T. Leijtens, L. M. Herz, A. Petrozza and H. J. Snaith, Electron-hole diffusion lengths exceeding 1 micrometer in an organometal trihalide perovskite absorber, *Science*, 2013, **342**, 341–344.

4 T. Swetha and S. P. Singh, Perovskite solar cells based on small molecule hole transporting materials, *J. Mater. Chem. A*, 2015, **3**, 18329–18344.

5 M. Urbani, G. De La Torre, M. K. Nazeeruddin and T. Torres, Phthalocyanines and porphyrinoid analogues as hole-and electron-transporting materials for perovskite solar cells, *Chem. Soc. Rev.*, 2019, **48**, 2738–2766.

6 Q. Chen, H. Zhou, Z. Hong, S. Luo, H. S. Duan, H. H. Wang, Y. Liu, G. Li and Y. Yang, Planar heterojunction perovskite solar cells via vapor-assisted solution process, *J. Am. Chem. Soc.*, 2014, **136**, 622–625.

7 G. E. Eperon, S. D. Stranks, C. Menelaou, M. B. Johnston, L. M. Herz and H. J. Snaith, Formamidinium lead trihalide: a broadly tunable perovskite for efficient planar heterojunction solar cells, *Energy Environ. Sci.*, 2014, **7**, 982–988.

8 J. Zhang, B. Xu, L. Yang, C. Ruan, L. Wang, P. Liu, W. Zhang, N. Vlachopoulos, L. Kloo, G. Boschloo, L. Sun, A. Hagfeldt and E. M. J. Johansson, Tailored electron transfer pathways in aucore/ptshell–graphene nanocatalysts for fuel cells, *Adv. Energy Mater.*, 2018, **8**, 1–12.

9 I. M. Abdellah, T. H. Chowdhury, J.-J. Lee, A. Islam, M. K. Nazeeruddin, M. Gräetzel and A. El-Shafei, Facile and low-cost synthesis of a novel dopant-free hole transporting material that rivals Spiro-OMeTAD for high efficiency perovskite solar cells, *Sustainable Energy Fuels*, 2021, **5**, 199–211.

10 B. Yadagiri, K. Narayanaswamy, T. H. Chowdhury, A. Islam, V. Gupta and S. P. Singh, Application of small molecules based on a dithienogermole core in bulk heterojunction organic solar cells and perovskite solar cells, *Mater. Chem. Front.*, 2020, **4**, 2168–2175.

11 J. Deng, W. Hu, W. Shen, M. Li and R. He, Exploring the electrochemical properties of hole transporting materials from first-principles calculations: an efficient strategy to improve the performance of perovskite solar cells, *Phys. Chem. Chem. Phys.*, 2019, **21**, 1235–1241.

12 Y. Wang, Q. Liao, J. Chen, W. Huang, X. Zhuang, Y. Tang, B. Li, X. Yao, X. Feng, X. Zhang, M. Su, Z. He, T. J. Marks, A. Facchetti and X. Guo, Teaching an old anchoring group new tricks: enabling low-cost, eco-friendly hole-transporting materials for efficient and stable perovskite solar cells, *J. Am. Chem. Soc.*, 2020, **142**, 16632–16643.

13 J. Zhou, X. Yin, Z. Dong, A. Ali, Z. Song, N. Shrestha, S. S. Bista, Q. Bao, R. J. Ellingson, Y. Yan and W. Tang, Dithieno [3, 2b: 2′, 3′d] pyrrole cored p-type semiconductors enabling 20% efficiency dopant-free perovskite solar cells, *Angew. Chem., Int. Ed.*, 2019, **58**, 13717–13721.

14 L. Liu, A. Mei, X. Li, H. Han, Y. Dkhissi, A. D. Scully, R. A. Caruso, Y. B. Cheng, I. Jeong, J. Lee, M. J. Ko, K. Yong, B. S. Richards, T. L. Kelly, N. Pellet, M. Levi, S. Turri, M. Levi and S. Turri, Incorporation of rubidium cations into perovskite solar cells improves photovoltaic performance, *Science*, 2016, **354**, 206–210.

15 Y. Hua, J. Zhang, B. Xu, P. Liu, M. Cheng, L. Kloo, E. M. J. Johansson, K. Sveinbjörnsson, K. Aitola, G. Boschloo and L. Sun, Facile synthesis of fluorene-based hole transport materials for highly efficient perovskite solar cells and solid-state dye-sensitized solar cells, *Nano Energy*, 2016, **26**, 108–113.

16 (*a*) S. M. Jain, Z. Qiu, L. Haggman, M. Mirmohades, M. B. Johansson, T. Edvinsson and G. Boschloo, Frustrated Lewis pair-mediated recrystallization of $CH_3NH_3PbI_3$ for improved optoelectronic quality and high voltage planar perovskite solar cells., *Energy Environ. Sci.*, 2016, **9**, 3770; (*b*) W. H. Nguyen, C. D. Bailie, E. L. Unger and M. D. McGehee, Enhancing the hole-conductivity of Spiro-OMeTAD without oxygen or lithium salts by using spiro$(TFSI)_2$ in perovskite and dye-sensitized solar cells, *J. Am. Chem. Soc.*, 2014, **136**, 10996.

17 (*a*) A. Dualeh, T. Moehl, N. Tétreault, J. Teuscher, P. Gao, M. K. Nazeeruddin and M. Grätzel, Impedance spectroscopic analysis of lead iodide perovskite-sensitized solid-state solar cells, *ACS Nano*, 2014, **8**, 362; (*b*) J. H. Heo and S. H. Im, $CH_3NH_3PbI_3$/poly-3hexylthiophen perovskite mesoscopic solar cells: Performance enhancement by Li-assisted hole conduction, *Phys. Status Solidi RRL*, 2014, **8**, 816; (*c*) H. Zhang, J. Cheng, D. Li, F. Lin, J. Mao, C. Liang, A. K. Y. Jen, M. Grätzel and W. C. H. Choy, Toward all room-temperature, solution-processed, high-performance planar perovskite solar cells: a new scheme of pyridine-promoted perovskite formation, *Adv. Mater.*, 2017, **29**, 1604695.

18 S. N. Habisreutinger, N. K. Noel, H. J. Snaith and R. J. Nicholas, Investigating the role of 4-*tert* butylpyridine in perovskite solar cells, *Adv. Energy Mater.*, 2017, **7**, 1601079.

19 B. Xu, Z. Zhu, J. Zhang, H. Liu, C.-C. Chueh, X. Li and A. K.-Y. Jen, 4-Tertbutylpyridine free organic hole transporting materials for stable and efficient planar perovskite solar cells, *Adv. Energy Mater.*, 2017, 1700683.

20 Y. Yue, N. Salim, Y. Wu, X. Yang, A. Islam, W. Chen, J. Liu, E. Bi, F. Xie, M. Cai and L. Han, Enhanced stability of perovskite solar cells through corrosion-free pyridine derivatives in hole-transporting materials, *Adv. Mater.*, 2016, **28**, 10738.

21 Y. Chen, X. Wan and G. Long, High performance photovoltaic applications using solution-processed small molecules, *Acc. Chem. Res.*, 2013, **46**, 2645–2655.
22 X. H. Zhu, J. Peng, Y. Cao and J. Roncali, Solution-processable single-material molecular emitters for organic light-emitting devices, *Chem. Soc. Rev.*, 2011, **40**, 3509–3524.
23 G. Benito, I. Zimmermann, J. Urieta-Mora, J. Aragó, J. Calbo, J. Perles, A. Serrano, A. Molina-Ontoria, E. Ortí, N. Martín and M. K. Nazeeruddin, Heteroatom effect on star-shaped hole-transporting materials for perovskite solar cells, *Adv. Funct. Mater.*, 2018, **28**, 1–10.
24 Y. Da Jiu, C. F. Liu, J. Y. Wang, W. Y. Lai, Y. Jiang, W. D. Xu, X. W. Zhang and W. Huang, Saturated and stabilized white electroluminescence with simultaneous three-color emission from a six-armed star-shaped single-polymer system, *Polym. Chem.*, 2015, **6**, 8019–8028.
25 W. D. Xu, W. Y. Lai, Q. Hu, X. Y. Teng, X. W. Zhang and W. Huang, A hydrophilic monodisperse conjugated starburst macromolecule with multidimensional topology as electron transport/injection layer for organic electronics, *Polym. Chem.*, 2014, **5**, 2942–2950.
26 M. Cheng, B. Xu, C. Chen, X. Yang, F. Zhang, Q. Tan, Y. Hua, L. Kloo and L. Sun, Phenoxazine-based small molecule material for efficient perovskite solar cells and bulk heterojunction organic solar cells, *Adv. Energy Mater.*, 2015, **5**, 1401720.
27 T. Swetha, M. Akhtaruzzaman, T. H. Chowdhury, N. Amin, A. Islam, T. Noda, H. M. Upadhyaya and S. P. Singh, Benzodithiazole-based hole-transporting material for efficient perovskite solar cells, *Asian J. Org. Chem.*, 2018, **7**, 2497–2503.
28 K. Narayanaswamy, B. Yadagiri, T. H. Chowdhury, T. Swetha, A. Islam, V. Gupta and S. P. Singh, Impact of A–D–A-structured dithienosilole- and phenoxazine based small molecular material for bulk heterojunction and dopant-free perovskite solar cells, *Chem. – Eur. J.*, 2019, **25**, 16320–16327.
29 B. Xu, J. Zhang, Y. Hua, P. Liu, L. Wang, C. Ruan, Y. Li, G. Boschloo, E. M. J. Johansson, L. Kloo, A. Hagfeldt, A. K. Y. Jen and L. Sun, Tailor-making low-cost spiro[fluorene-9,9′-xanthene]-based 3D oligomers for perovskite solar cells, *Chem*, 2017, **2**, 676–687.
30 W. Yu, J. Zhang, D. Tu, Q. Yang, X. Wang, X. Liu, F. Cheng, Y. Qiao, G. Li, X. Guo and Li. A Can, spirobixanthene-based dendrimeric hole-transporting material for perovskite solar cells, *Sol. RRL*, 2019, 1900367.
31 N. K. Noel, A. Abate, S. D. Stranks, E. S. Parrott, V. M. Burlakov, A. Goriely and H. J. Snaith, Enhanced photoluminescence and solar cell performance *via* Lewis base passivation of organic–inorganic lead halide perovskites, *ACS Nano*, 2014, **8**, 9815.
32 M. Dürr, A. Yasuda and G. Nelles, On the origin of increased open circuit voltage of dye-sensitized solar cells using 4-*tert*-butyl pyridine as additive to the electrolyte, *Appl. Phys. Lett.*, 2006, **89**, 061110.
33 Y. Wang, W. Liu, J. Deng, G. Xie, Y. Liao, Z. Qu, H. Tan, Y. Liu and W. Zhu, Engineering the interconnecting position of star-shaped donor-π-acceptor molecules based on triazine, spirofluorene, and triphenylamine moieties for color tuning from deep blue to green, *Chem. – Asian J.*, 2016, **11**, 2555–2563.
34 G. Tumen-Ulzii, T. Matsushima, D. Klotz, M. R. Leyden, P. Wang, C. Qin, J.-W. Lee, S.-J. Lee and C. Yang,Y.; Adachi, Hysteresis-less and stable perovskite solar cells with a self-assembled monolayer, *Commun. Mater.*, 2020, **1**, 1–7.
35 J. A. Rohr, X. Shi, S. A. Haque, T. Kircharts and J. Nelson, Charge transport in spiro-OMeTAD investigated through space-charge-limited current measurements, *Phys. Rev. Appl.*, 2018, **9**, 044017.